The consequence of fiber orientation downsampling on the computation of white matter tract-related deformation

Zhou Zhou,[1] Teng Wang, [1] Xiaogai Li[1]

[1] Neuronic Engineering, KTH Royal Institute of Technology, Stockholm, 14152, Sweden.

[*] Corresponding author. Email: zhouz@kth.edu

Author information

Zhou Zhou, Division of Neuronic Engineering, Royal Institute of Technology (KTH), SE-14152, Huddinge, Sweden, Email: zhouz@kth.se

Teng Wang, Division of Neuronic Engineering, Royal Institute of Technology (KTH), SE-14152, Huddinge, Sweden, Email: tenwan@kth.se

Xiaogai Li, Division of Neuronic Engineering, Royal Institute of Technology (KTH), SE-14152, Huddinge, Sweden, Email: xiaogai@kth.se

Abstract

Incorporating neuroimaging-revealed structural details into finite element (FE) head models opens vast opportunities to understand brain injury mechanisms. Recently, growing efforts have been made to integrate the fiber orientation from diffusion tensor imaging into the FE models to compute white matter (WM) tract-related deformation. Commonly used approaches often downsample the spatially enriched fiber orientation to match the resolution of FE meshes, resulting in an element-wise orientation implementation. However, the validity of downsampling and the consequences on the computed tract-related strains remain elusive. To address this problem, the current study proposed a new voxel-wise approach to integrate fiber orientation into FE models without downsampling. By setting the voxel-wise orientation responses as the reference, we then evaluated the reliability of two existing downsampling approaches on tract-related strains using two FE models with varying element sizes. The results showed that, for a model with a large mesh-image resolution dismatch, the downsampling orientation exhibited an absolute difference over 30° across the WM/gray matter interface and pons regions and further negatively affects the computation of tract-related strains with the normalized root-mean-square error up to 20% and peaking tract-related strains underestimated by 5%. This downsampling-induced effect was lower in FE models with finer meshes. Thus, this study yields insights on integrating neuroimaging-revealed fiber orientation into FE models and may better inform the computation of WM tract-related deformation, which are crucial for advancing the etiological understanding and computational predictability of brain injury.

Keywords

Finite element analysis; resolution mismatch; fiber orientation downsampling; tract-related strains; traumatic brain injury

Graphic Abstract

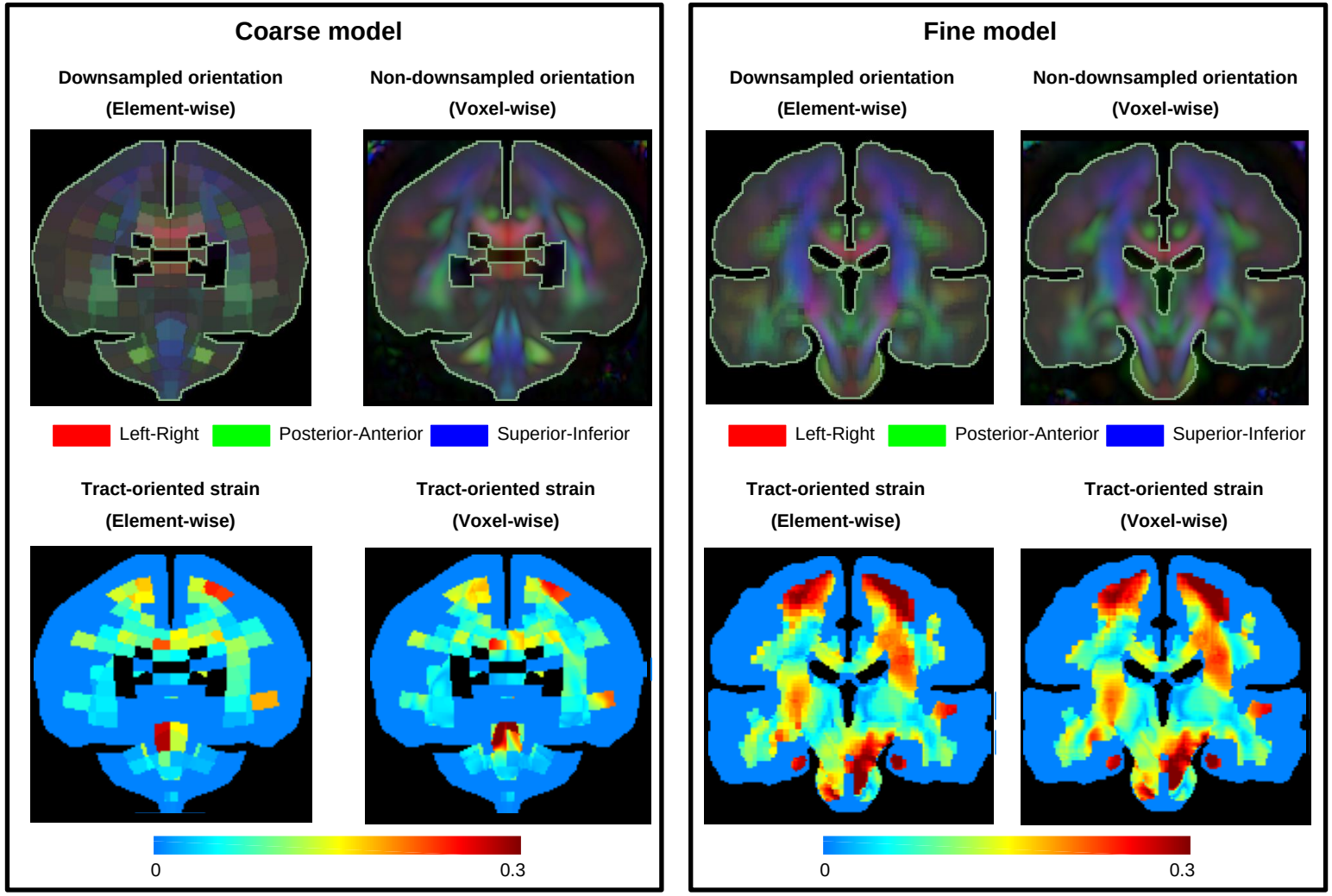

Highlights

- A new approach was proposed to integrate voxel-wise fiber orientation delineated by diffuseion tensor imaging into finite element models.
- The commonly used orientation downsampling caused a systematic loss of orientation information and further compromised the computation of white matter tract-related deformation, particularly for the coarsely meshed model.
- The downsampling-induced effect was lower in heavily discretized models

Introduction

Traumatic brain injury (TBI) is a disruption in the brain's normal function secondary to an external insult to the head, typically in the form of head impact and inertial loading. Depending on the severity of insults, the outcome of TBI may vary from temporal unconsciousness accompanied by transient neuronal circuit dysfunction, e.g., concussion (Wolf et al., 2017), to persistent vegetative state along with profound neuronal apoptosis throughout the white matter (WM), e.g., diffuse axonal injury (Maxwell et al., 2003). Given its high morbidity and mortality and the large number of people affected (Brazinova et al., 2021; Peterson et al., 2019), TBI is a critical public health and socio-economic threat worldwide. Therefore, a fundamental understanding of TBI pathogenesis is pivotal to reduce the occurrence and alleviate its consequence.

Finite element (FE) models are computational surrogates of the human head, which accounts for the geometrical and mechanical features of various intracranial components, as well as the interfacial conditions among them. Many FE models have been established over the past decades in light of their immerse potentials to explore the pathomechanical cascades from external insults, localized tissue responses, and resultant brain injury (see review articles (Giudice et al., 2019; Madhukar and Ostoja-Starzewski, 2019; Yang and Mao, 2019)). Particularly, advances in neuroimaging have largely facilitated anatomically authentic presentations of various structures in contemporary head models. For example, by leveraging high-resolution computed tomography scans and angiography, several three-dimensional (3D) head models have successfully captured the cranial morphology (De Kegel et al., 2019; Li et al., 2017, 2019) and cerebral vasculature (Ho and Kleiven, 2007; Subramaniam et al., 2021; Zhao and Ji, 2020), respectively. Such FE models often require fine meshes to resolve the geometrical complexities appropriately. For instance, two recent brain models with conforming hexahedral meshes that captured the morphological heterogeneity of the cerebral cortex (i.e., gyri and sulci) and lateral ventricles exhibited a mean mesh size of 0.85 mm with up to 1.2 million elements for the brain (Li et al., 2021; Zhou et al., 2019b). For head models with smoothed brain

surfaces, brain elements varied from 5 k to 202 k with mesh resolutions of 1.8 - 6 mm (Chatelin et al., 2011; Kleiven and von Holst, 2002; Mao et al., 2013; Zhao and Ji, 2019a).

Partially inspired by the experimental findings that functional impairment and morphological damage of axonal fibers were relevant to the strain regime imposed on the experimental tissue (LaPlaca et al., 2007; Montanino, 2020; Morrison III et al., 2011; Wu et al., 2021b), the fiber orientation delineated by diffusion tensor imaging (DTI) has been integrated into FE models in recent years to inform the computation of tract-related deformation. Thus far, various techniques have been proposed to integrate the DTI-delineated fiber orientation into FE models. For example, Zhou et al. (2021a) obtained the deformation along the fiber tracts by projecting the strain tensor along the real-time orientation of fiber tracts (i.e., tract-oriented strain), while Giordano et al. (2014) instead simulated the brain as a hyper-viscoelastic fiber-reinforced anisotropic medium with the fiber orientation integrated into the constitutive law to inform the fiber reinforcement. Owning to the resolution mismatch between FE brain elements and DTI voxels, the fiber orientation from multiple voxels was downsampled to one artificial orientation per element in these two techniques (collectively referred to as element-wise orientation implementation, hereafter). Similar or the same element-wise orientation implementation have been used in other studies (Chatelin et al., 2011; Colgan et al., 2010; Giordano and Kleiven, 2014; Giordano et al., 2017; Hernandez et al., 2019; Kraft and Dagro, 2011; Kraft et al., 2012; Laksari et al., 2020; Sahoo et al., 2016; Sullivan et al., 2015; Zhao and Ji, 2019b; Zhou et al., 2021b). To circumvent the orientation downsampling, Garimella et al. (2019) explicitly incorporated the whole WM fiber tractography reconstructed from DTI into a head model in which multiple fibers were embedded within one WM element, while Ji et al. (2015) transformed the fiber orientation of WM voxels from the DTI space into the coordinate system of the FE head model then computed the tract-oriented strain at the voxel level by resolving the strain tensor of the WM element from pre-computed simulation to the fiber orientation of these transformed voxels. Regardless of these above-described disparities incorporating WM fiber orientation along with other model-specific choices, maximum tract-oriented strain (alternatively termed as axonal strain or fiber strain in the

95 literature) has been congruently reported as an appropriate measure of injury by several independent
96 groups (Giordano and Kleiven, 2014; Wu et al., 2021a; Zhao et al., 2017; Zhou et al., 2021b). More
97 recently, Zhou et al. (2021b) related strain tensors of WM elements to the real-time fiber direction and
98 proposed three new tract-related strain metrics, measuring the normal deformation perpendicular to
99 the fiber tracts (i.e., tract-perpendicular strain), and shear deformation along and perpendicular to the
100 fiber tracts (i.e., axial-shear strain and lateral-shear strain, respectively). All of them exhibited superior
101 injury predictability over maximum principal strain.

102 Given that the computation of any tract-related strains is directly dependent on the fiber
103 orientation, appropriate integration of fiber orientation into FE models is crucial. When limiting to the
104 element-wise orientation implementation involving orientation downsampling to match the resolution
105 of finite element and imaging voxel, the validity of such implementation has not been appropriately
106 evaluated. For example, Giordano et al. (2014) averaged the fiber orientation obtained from DTI with
107 a resolution of 2 mm × 2 mm × 3.6 mm to match the resolution of an FE model with an average element
108 size of 5 mm. Similarly, Sahoo et al. (2014) downsampled the fiber orientation from a DTI atlas with an
109 isotropic resolution of 1 mm^3 for another FE model with mesh sizes ranging from 1.14 mm to 7.73 mm.
110 Nevertheless, neither have quantitatively compared the downsampled orientation information with
111 its counterparts convey in the DTI and how the downsampling procedures affect the FE-derived tract-
112 related deformation remains to be systematically ascertained.

113 Thus, the aim of the current study is to quantitatively evaluate the consequence of orientation
114 downsampling on the computed WM tract-related deformation. To achieve this, a new approach was
115 developed to integrate the voxel-wise fiber directions into FE models. This new approach and two
116 existing downsampling algorithms were respectively implemented into two FE head models with
117 varying levels of mesh sizes. By setting the responses determined by the voxel-wise implementation
118 as the reference, the reliability of two rival downsampling approaches was quantitatively evaluated.
119 We thus tested the hypothesis that orientation downsampling discredits the FE-derived tract-related
120 strains, particularly for the model with a higher mesh-imaging resolution mismatch.

Methods

Finite element head models

Two previously developed head models with varying mesh resolutions were used in this study, i.e., the KTH model (Kleiven, 2007) (**Fig. 1A-B**) and the ADAPT model (Li et al., 2021) (**Fig. 1C-D**). Each model consists of critical head components, including gray mater, WM, skull, scalp, subarachnoid cerebrospinal fluid (CSF), ventricles, superior sagittal sinus, transverse sinus, meninges, falx, and tentorium. The brain in both models was discretized by hexahedral elements with spatially heterogeneous element size. Following the tissue classification protocol proposed by Zhou et al. (2021b), the KTH model includes 1197 WM elements with a resolution of 6.23 ± 1.93 mm (range of 1.93 - 11.35 mm); the ADAPT model contains 113678 WM elements with a mesh size of 0.85 ± 0.35 mm (range of 0.25 - 3.25 mm). Further details about the geometrical discretization and mesh quality can be found in previous studies (Kleiven and von Holst, 2002; Li et al., 2021). Responses of both models have shown good correlation with experiments of brain strain, brain-skull relative motion, and intracranial pressure (Kleiven, 2006; Li et al., 2021; Zhou et al., 2019c; Zhou et al., 2019d; Zhou et al., 2018). Both models have been used to uncover the brain injury mechanism (Kleiven and von Holst, 2002; Li, 2021; Zhou et al., 2019a), evaluate the brain injury risk (Kleiven, 2007; Zhan et al., 2021), and inform the contrivance of advanced protective devices and treatment strategies (Fahlstedt et al., 2021; Wang et al., 2020).

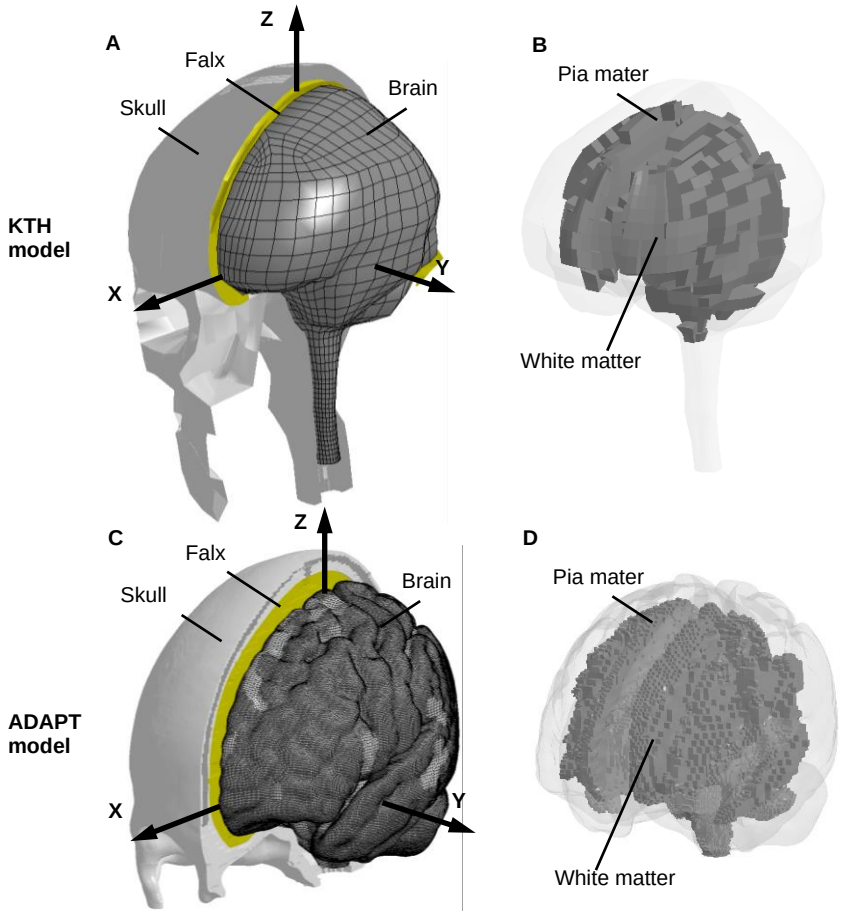

Fig. 1. Two finite element head models with varying mesh resolutions. For the KTH head model with relatively coarse mesh, an isometric view of the head with the skull open to expose the brain is presented in subfigure (**A**) in which a skull-fixed coordinate system with the origin at the head's center of gravity, while the pia mater and white matter are shown in subfigure (**B**) with the pia mater in translucency. Similar views are presented for the ADAPT head model with relatively fine mesh in subfigures (**C**) and (**D**). The brain FE elements are shown with mesh outlines in subfigures (**A**) and (**C**) to illustrate the mesh resolution.

Implementation of element-wise fiber orientation into FE brain models

To compute WM fiber tract-related deformation, the fiber orientation from an open-accessed ICBM DTI-81 atlas (dimensions 181 × 217 × 181, 1 mm isotropic) (Mori et al., 2008) was integrated into the two brain models at an element-wise basis using two previously proposed downsampling approaches. As is common in both approaches, the FE brain mesh for each head model was voxelized to obtain a reference volume, which was further aligned with the brain volume of the ICBM DTI-81 atlas via a diffeomorphic Demon registration (Li et al., 2021). Then, for each WM element in brain models, corresponding voxels in the DTI atlas enclosed by the given element were distinguished. To integrate the fiber orientation from multiple voxels into each WM element, either the first eigenvectors of the diffusion tensors or the diffusion tensors themselves in these identified voxels

were respectively downsampled using equations (1) (referred to as vector-averaged approach) and (2) (referred to as tensor-averaged approach) via a distance-weighted averaging scheme, in which the information from those voxels closer to the centroid of the element was more heavily weighted:

$$\boldsymbol{v}_{elem} = \frac{\sum_{i=1}^{N} \boldsymbol{v}_i e^{-D_i}}{\sum_{i=1}^{N} e^{-D_i}} \tag{1}$$

$$\boldsymbol{T}_{elem} = \frac{\sum_{i=1}^{N} \boldsymbol{T}_i e^{-D_i}}{\sum_{i=1}^{N} e^{-D_i}} \tag{2}$$

where $\boldsymbol{v}_{elem}$ and $\boldsymbol{T}_{elem}$ are respectively the mean first eigenvector and the mean diffusion tensor calculated for each WM element; N is the number of selected voxels for each WM element; $\boldsymbol{v}_i$ and $\boldsymbol{T}_i$ are respectively the first eigenvector and diffusion tensor of each selected voxel; D_i is the distance from the voxel to the element centroid. Note that, before the implementation of equation (1), the angle between $\boldsymbol{v}_i$ and a preselected reference vector (i.e., the $\mathbf{X}$-axis in the skull-fixed coordinate system in **Fig. 1** in the current study) were examined. Under the condition that the angle was greater than 90°, the $\boldsymbol{v}_i$ would be flipped (i.e., -$\boldsymbol{v}_i$). As highlighted by Zhao and Ji (2019b), such a flip operation was needed since fiber orientation is expressed with either $\boldsymbol{v}_i$ or -$\boldsymbol{v}_i$, and it is necessary to ensure the consistency in the eigenvector across all the voxels and circumvent improper cancelation in equation (1).

The resultant orientation from equations (1) and (2) was respectively implemented at an element-wise basis. For the vector-averaged approach (equation 1), the $\boldsymbol{v}_{elem}$ was considered the mean fiber orientation for each element (**Fig. 2A**), similar to the approach in Chatelin et al. (2011) and Zhao and Ji (2019b). For the tensor-weighted approach (equation 2), the first eigenvector of the $\boldsymbol{T}_{elem}$ was regarded as the mean orientation for each element (**Fig. 2B**), the same as the strategies in Zhou et al. (2021b) and Giordano et al. (2014).

Implementation of voxel-wise fiber orientation into FE brain models

To circumvent the downsampling procedures, the fiber direction in DTI voxels was directly implemented to the FE models. Same as these two downsampling approaches described above, DTI voxels enclosed by each WM element were identified at first based on their spatial correspondence.

For each WM element, the first eigenvectors of all identified voxels (i.e., $\boldsymbol{v}_i$ in equation (1)) were wholly embedded into a given element without downsampling. Thus, the fiber orientation was implemented at a voxel-wise basis (referred to as the voxel-wise approach hereafter) with an isotropic resolution of 1 mm^3 with the resultant orientation map shown in **Fig. 2C.**

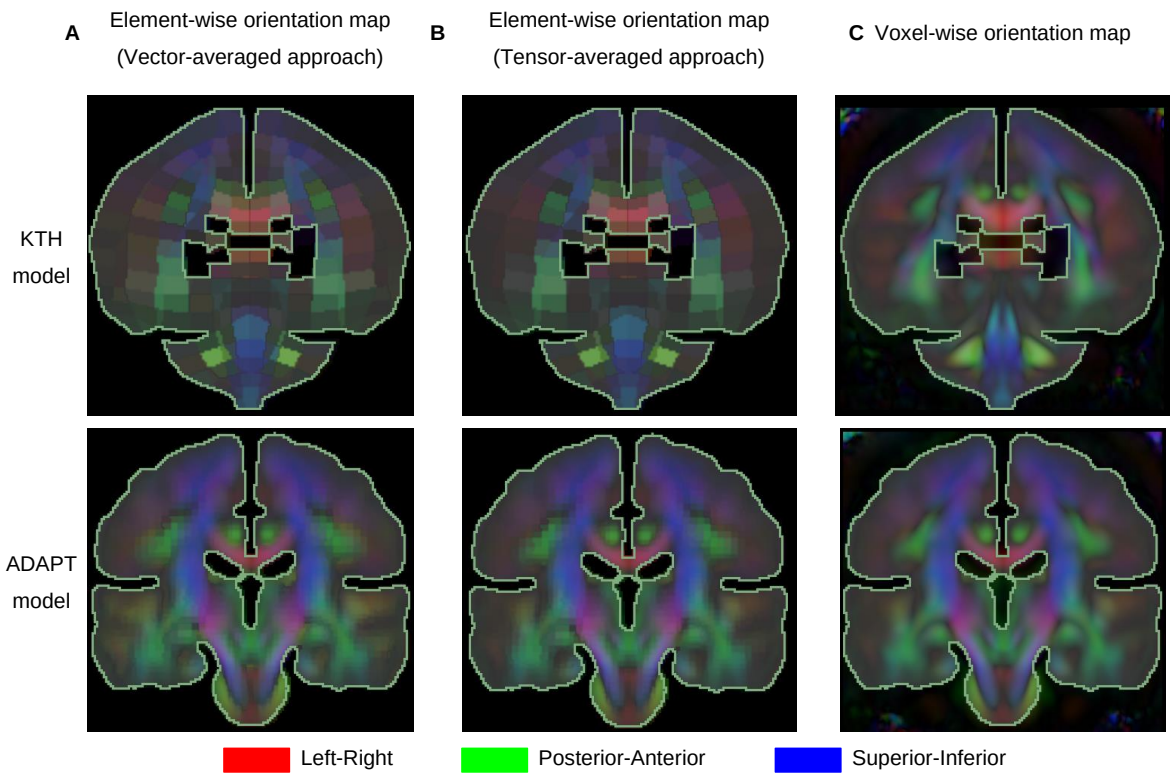

Fig. 2. Color-coded orientation maps implemented either at an element-wise basis using the vector-averaged approach (**A**) and tensor-averaged approach (**B**) or at a voxel-wise basis using the voxel-wise approach (**C**). The outline of the brain mask with the differentiation of ventricles used for image registration is superimposed to the orientation map.

Real-time fiber orientation for the computation of tract-related strains

To inform the computation of tract-related strains with real-time fiber orientation, an embedded element approach was leveraged to track the real-time fiber orientation following the approach presented earlier (Zhou et al., 2021a). For all the three above-mentioned approaches, the orientation information was concretely represented by truss elements (serving as slave elements) which were embedded within the WM elements (serving as master elements). Note that the truss elements only served as instruments to monitor the updated orientation of fiber tracts at each time step without additional contribution to mechanical stiffness (Zhou et al., 2021a). For both the vector-averaged and tensor-averaged approaches, only one truss element was embedded per WM element.

In particular, for the vector-averaged approach, the truss element is oriented in the same direction as that of $\boldsymbol{v}_{elem}$, while, for the tensor-averaged approach, the direction of the truss elements is aligned with the first eigenvector of the $\boldsymbol{T}_{elem}$. For the voxel-wise approach, multiple truss elements were embedded in one WM element, in which truss elements angled along the direction of the first eigenvector of those voxels (i.e., $\boldsymbol{v}_i$ in equation (1)) within the given element. As is common across the three approaches, both ends of the truss elements fell within the boundaries of their master elements by adjusting the length of the embedded truss elements. Thus, nodal motion of a given truss element was governed exclusively by its master element. Consequently, the real-time fiber orientation during head impacts was reflected by the temporal direction of the truss element, which was updated at each solution cycle of the time-marching simulation.

To compute the deformation associated with the fiber tracts, both the Green-Lagrange strain tensors for all WM elements and the orientation of the embedded truss elements were obtained for each timestep from pre-computed simulations and then transformed into the skull-fixed coordinate system. The strain tensor of each WM element was further rotated to the coordinate systems with one axis aligned with the real-time fiber orientation, through which four strain-based metrics relating to the fiber deformation were extracted (**Fig. 3**), i.e., tract-oriented strain, tract-perpendicular strain, axial-shear strain, and lateral-shear strain. For the vector-averaged approach, the strain tensor of each WM element was only related to one real-time fiber orientation, which is also the case for the tensor-averaged approach. For the voxel-wise approach, the strain tensor of one given WM element was related to the temporal direction of all the truss elements encased by the given WM element.

The implementation of the embedded element method for tracking the real-time fiber orientation and the computation of four tract-related strains are described with greater details in Zhou et al. (2021a) and Zhou et al. (2021b), respectively.

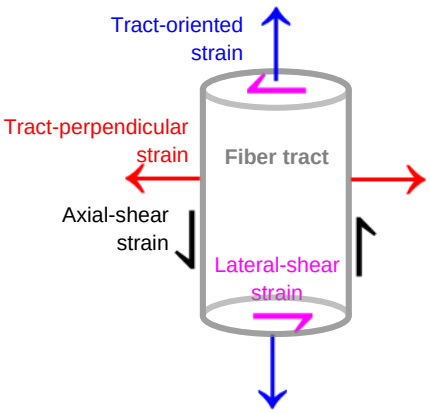

Fig. 3. Illustration of the four tract-related strains with respect to the fiber tract. Tract-oriented strain and tract-perpendicular strain measure the normal deformation along and perpendicular to the fiber tracts, while axial-shear strain and lateral-shear strain measure shear deformation along and perpendicular to the fiber tracts.

Impact simulation

To study the influence of fiber orientation downsampling on the computation of tract-related deformation, a concussive impact (i.e., case 157H2) from the National Football League dataset (Sanchez et al., 2019) was simulated using the KTH model and the ADAPT model with embedded fiber orientation implemented by the vector-averaged approach, tensor-averaged approach, and voxel-wise approach, respectively. In case157H2, the football player was laterally struck, resulting in high angular velocities in the coronal and sagittal planes, which is typically associated with brain injury. In the simulation, the translational and rotational velocities were prescribed to the rigid skull with the velocity profiles expressed with respect to the skull-fixed coordinate system. The impact was recorded for 50 ms, which took 4 hours for the KTH model and 67 hours for the ADAPT model to solve using a massively parallel processing version of LS-DYNA with 128 CPUs. The model responses were output at every 1 ms.

Data analysis

Identical to that of the orientation information (concretely represented by the truss elements) being integrated into FE models, the spatial resolution of FE-derived response was at the voxel level for the voxel-wise approach and at the element level for the vector- and tensor-averaged approaches. To address this disparity, all responses were mapped back to the imaging space of the ICBM DTI-81 atlas. This was intuitive for the voxel-wise approach, given that a one-to-one correspondence between

the voxel and truss element was established. For the tensor- and vector-averaged approaches in which multiple voxels corresponded to one element, the response of a WM element was assigned to all the voxels enclosed by the given element. Such mapping operations synchronized the response resolutions and facilitated direct comparisons among the three approaches. Response-encoded contours were generated in the imaging space.

To quantify the local fiber orientation embedded within the FE models, the skull-fixed coordinate system was selected as the reference. Adapting the strategy by Giordano et al. (2017), the fiber orientation was expressed in terms of two Eulerian angles, i.e., elevation angle (α) and azimuth angle (β) (**Fig. 4, Table 1A**). To identify the localized alteration of fiber orientation associated with the downsampling procedures by either the vector- or tensor-averaged approaches, the absolute differences in elevation angle and azimuth angle between the voxel-wise approach and each of the two downsampling approaches were calculated at the voxel-wise level, respectively (**Table 1B**).

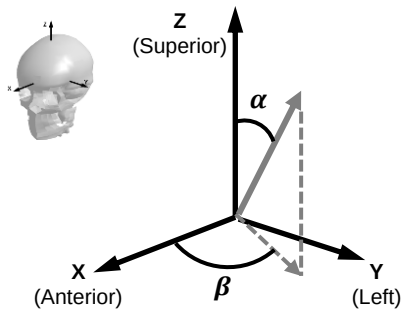

Fig. 4. Characterization of the fiber orientation (gray arrow in solid line) by means of elevation angle ($\alpha \in [0°, 90°]$) and azimuth angle ($\beta \in [0°, 90°]$). These angles are expressed with respect to the skull-fixed coordinate system with a whole-head thumbnail on the top-left corner.

To further evaluate the consequence of orientation downsampling on the computation of fiber deformation, four tract-related strains (**Fig. 3** and **Table 1A**) were extracted from FE models with the real-time fiber orientation described above. For each of the four strains, the absolute difference between the voxel-wise approach and two downsampled approaches was respectively calculated per voxel (**Table 1B**) and was further expressed in the form of normalized root-mean-square error (NRMSE; normalized by the mean value determined by the voxel-wise approach). To quantify the influence of the orientation downsampling on the peaking strain responses, the 95th percentile maximum values of

four tract-related strains were extracted across the whole WM. All data analyses were performed in MATLAB (2016b; Mathworks, Natick, MA).

Table 1 – Summary of variables quantifying the fiber orientation implemented by three rival approaches and tract-related strains (**A**) and expression quantifying the absolute differences associated with the orientation downsampling (**B**). In each variable, the subscript indicates the basis that the orientation information is implemented (i.e., vxl for the voxel-wise basis, elm for the element-wise basis), while the superscript indicates the orientation downsampling approaches (i.e., v for vector-averaged approach, T for tensor-averaged approach).

A	**Variable**	**Description**
	$\alpha_{vxl}/\alpha_{elm}^{v}/\alpha_{elm}^{T}$	Elevation angle of the undeformed fiber orientation implemented by voxel-wise approach, vector-averaged approach, and tensor-averaged approach, respectively.
	$\beta_{vxl}/\beta_{elm}^{v}/\beta_{elm}^{T}$	Azimuth angle of the undeformed fiber orientation implemented by voxel-wise approach, vector-averaged approach, and tensor-averaged approach, respectively.
	$MTOS_{vxl}/MTOS_{elm}^{v}/MTOS_{elm}^{T}$	Peak of tract-oriented strain across the entire simulation with the fiber orientation implemented by voxel-wise approach, vector-averaged approach, and tector-averaged approach, respectively.
	$MTPS_{vxl}/MTPS_{elm}^{v}/MTPS_{elm}^{T}$	Peak of tract-perpendicular strain across the entire simulation with the fiber orientation implemented by voxel-wise approach, vector-averaged approach, and tensor-averaged approach, respectively.
	$MASS_{vxl}/MASS_{elm}^{v}/MASS_{elm}^{T}$	Peak of axial shear strain across the entire simulation with the fiber orientation implemented by voxel-wise approach, vector-averaged approach, and tensor-averaged approach, respectively.
	$MLSS_{vxl}/MLSS_{elm}^{v}/MLSS_{elm}^{T}$	Peak of lateral shear strain across the entire simulation with the fiber orientation implemented by voxel-wise approach, vector-averaged approach, and tensor-averaged approach, respectively.
B	**Expression**	**Description**
	$\lvert\alpha_{vxl} - \alpha_{elm}^{v}\rvert/\lvert\alpha_{vxl} - \alpha_{elm}^{T}\rvert$	Absolute difference in elevation angle between the voxel-wise approach and each of the two downsampling approaches, respectively.
	$\lvert\beta_{vxl} - \beta_{elm}^{v}\rvert/\lvert\beta_{vxl} - \beta_{elm}^{T}\rvert$	Absolute difference in azimuth angle between the voxel-wise approach and each of the two downsampling approaches, respectively.
	$\lvert MTOS_{vxl} - MTOS_{elm}^{v}\rvert/$ $\lvert MTOS_{vxl} - MTOS_{elm}^{T}\rvert$	Absolute difference in maximum tract-oriented strain between the voxel-wise approach and each of the two downsampling approaches, respectively.
	$\lvert MTPS_{vxl} - MTPS_{elm}^{v}\rvert/$ $\lvert MTPS_{vxl} - MTPS_{elm}^{T}\rvert$	Absolute difference in maximum tract-perpendicular strain between the voxel-wise approach and each of the two downsampling approaches, respectively.
	$\lvert MASS_{vxl} - MASS_{elm}^{v}\rvert/$ $\lvert MASS_{vxl} - MASS_{elm}^{T}\rvert$	Absolute difference in maximum axial-shear strain between the voxel-wise approach and each of the two downsampling approaches, respectively.
	$\lvert MLSS_{vxl} - MLSS_{elm}^{v}\rvert/$ $\lvert MLSS_{vxl} - MLSS_{elm}^{T}\rvert$	Absolute difference in maximum axial-shear strain between the voxel-wise approach and each of the two downsampling approaches, respectively.

Results

To illustrate the extent of orientation downsampling in both brain models, the number of voxels identified for each WM element was examined. For the KTH model, the number of voxels per WM element was 312 ± 198 (range of 6-980) (**Fig. 5A**). For the ADAPT model, a mean of 3 voxels (range of 1-57) was identified for a typical WM element (**Fig. 5B**). Consequently, 1197 truss elements were respectively embedded per the implementation of vector- and tensor-averaged approaches, while 373976 truss elements for the voxel-wise approach for the KTH model (**Fig. 5C**). For the ADAPT model, the numbers of truss elements introduced by both downsampling approaches were 113678, in comparison with 433299 by the voxel-wise approach (**Fig. 5D**).

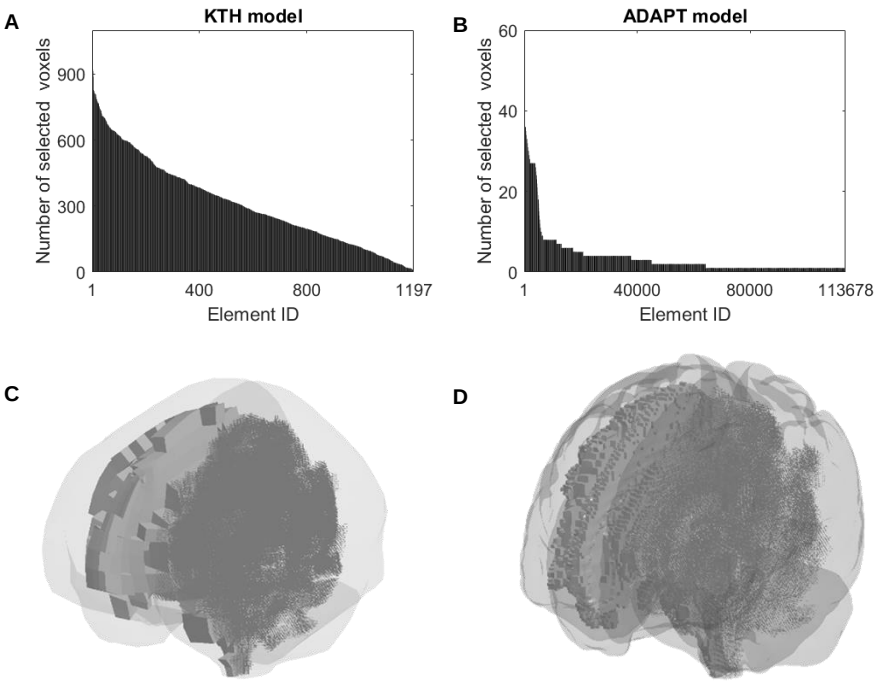

Fig. 5. Number of DTI voxels selected for each of the WM element (**A**-**B**) and brain model with WM elements and embedded truss elements implemented by the voxel-wise approach (**C**-**D**) in the KTH model (left column) and ADAPT model (right column). For better illustration, the brain model in subfigures (**C**) and (**D**) is shown in translucency with the WM element in only one hemisphere being visible.

For an exemplary WM element in the KTH model (**Fig. 6A-C**) encasing 361 voxels, the mean values for α_{vxl} and β_{vxl} in the voxel-wise approach were 64.1° (range of 47.8° - 89.5°) and 66.3° (range of 54.6° - 73.3°), respectively. Due to downsampling, the resultant elevation and azimuth angles were 66.7° (α_{elm}^{v}) and 66.2°(β_{elm}^{v}) for the vector-averaged approach, and 61.9°(α_{elm}^{T}) and 64.8°(β_{elm}^{T}) for the tensor-averaged approach, all of which fell within the range measured from the voxel-wise approach (**Fig. 6B**). Similarly, the range of each tract-related strain calculated from the voxel-wise

295 approach covered its counterparts by the two downsampling approaches. Using the results
296 determined by the voxel-wise approach as the reference, the NRMSE values ranged from 7.3% in MASS
297 to 21.9% in MTOS for the vector-averaged approach, and from 6.5% in MASS to 22.9% in MTOS for the
298 tensor-averaged approach (**Fig. 6C**).

299 A similar analysis was performed on an exemplary element enclosing 36 voxels in the ADAPT
300 head model (**Fig. 6D-F**). All the response variables of interest determined by the voxel-wise approach
301 covered their counterparts from the two downsampling approaches. For fiber orientation, the voxel-
302 wise approach (**Fig. 6D**) exhibited a range of 38.9° – 47.1° for α_{vxl} (mean value: 42.3°) and 49.6° - 58.8°
303 for β_{vxl} (mean value: 53.1°), while fiber angles measured from the vector- and tensor-averaged
304 approaches were commensurable with each other (i.e., α_{elm}^{v}: 42.3° vs. α_{elm}^{T}: 42.3°; β_{elm}^{v}: 53.1° vs.
305 β_{elm}^{T}: 52.9°) (**Fig. 6E**). For the strain-based metrics, the two downsampling approaches lead to nearly
306 identical values in all four tract-related strains (**Fig. 6F**). The NRMSE values for the tensor-average
307 approach spanned from 1.1% (MASS) to 7.3% (MTOS) comparing with the voxel-wise approach. The
308 same NRMSE values were also noted for the vector-average approach when limiting to the precision
309 as one digital.

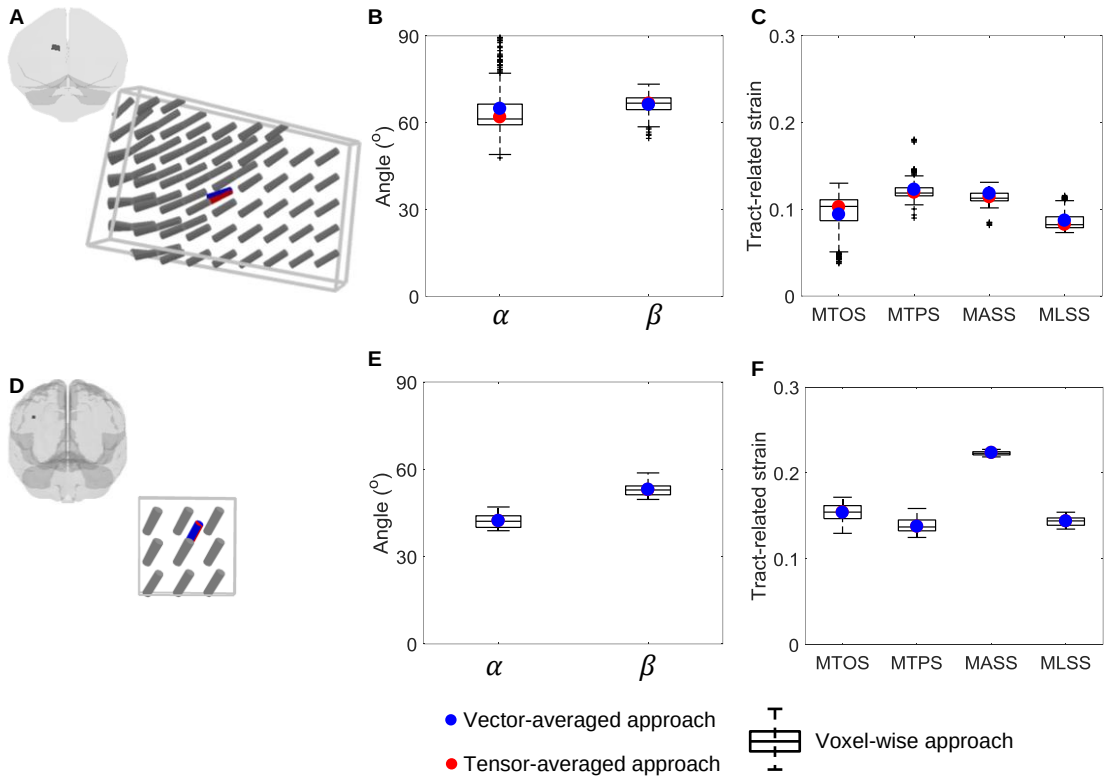

Fig. 6. (**A**) Embedded truss elements implemented in an exemplary WM element in the KTH model with a whole-head thumbnail showing the view angle. The truss elements are coloured in blue and red for the vector- and tensor-averaged approaches, respectively, while in gray for the voxel-wise approach. (**B**) Boxplots of elevation angle (α) and azimuth angle (β) of the truss elements in subfigure (**A**). (**C**) Boxplots of four tract-related strains for the exemplary element in subfigure (**A**). Similar figures are also shown for one exemplary WM element in ADAPT model in subfigures (**D**-**F**) in the right column. Note that in subfigures (**A**) and (**B**), the exemplary WM element enclosed 361 voxels for the KTH model and 32 voxels for the ADAPT model. Thus, some of the truss elements (in grey) implemented by the voxel-wise approach were overlapped with each other from the given view angles.

The above-described analysis illustrated by one exemplified element per model was extended to the whole WM. In both models, the three approaches resulted in similar distributions of α in the deep brain regions, such as the corpus callosum with the α consistently around 90°. Nevertheless, in the KTH model, the absolute differences in α over 30° due to orientation downsampling exhibited patchy distribution, spreading across the WM/gray matter interface and pons regions (highlighted in **Fig. 7A**). Such patchy-distributed differences were not seen in the ADAPT model with relatively fine meshes, in which only a handful of isolated voxels with absolute differences in α over 30° were revealed. Similar trends were also noted in β (**Fig. A1** in Appendix).

To evaluate the consequence of orientation downsampling on the computation of fiber deformation, four tract-related strains were calculated from both models with the fiber orientation

either directly implemented at the voxel-wise level or downsampled to the element-wise level. For the MTOS (**Fig. 7B**), both downsampling approaches introduced considerable differences (i.e., absolute difference exceeding 0.1) in the KTH model, particularly in the pons regions. In the ADAPT model, only a few voxels have absolute differences over 0.1. This was further confirmed by the NRMSR value based on MTOS calculated at the whole WM region (**Table 2**). For the vector- and tensor-averaged approaches, the NRMSE values were 33.0% and 32.7% for the KTH model, while 4.2% and 4.8% for the ADAPT model. Similar trends were also noted for the other three tract-related strains (**Fig. A2** in Appendix). Quantitatively, the NRMSE values of other three tract-related strains in the KTH model ranged from 20.3% (MLSS) to 25.0% (MTPS) for the vector-averaged approach, and from 20.2% (MLSS) to 24.5% (MTPS) for the tensor-averaged approach. Consistent with that of MTOS, the NRMSE values for the other three tract-related strains in the ADAPT model were consistently less than 5% both for the vector- and tensor-averaged approaches (**Table 2**).

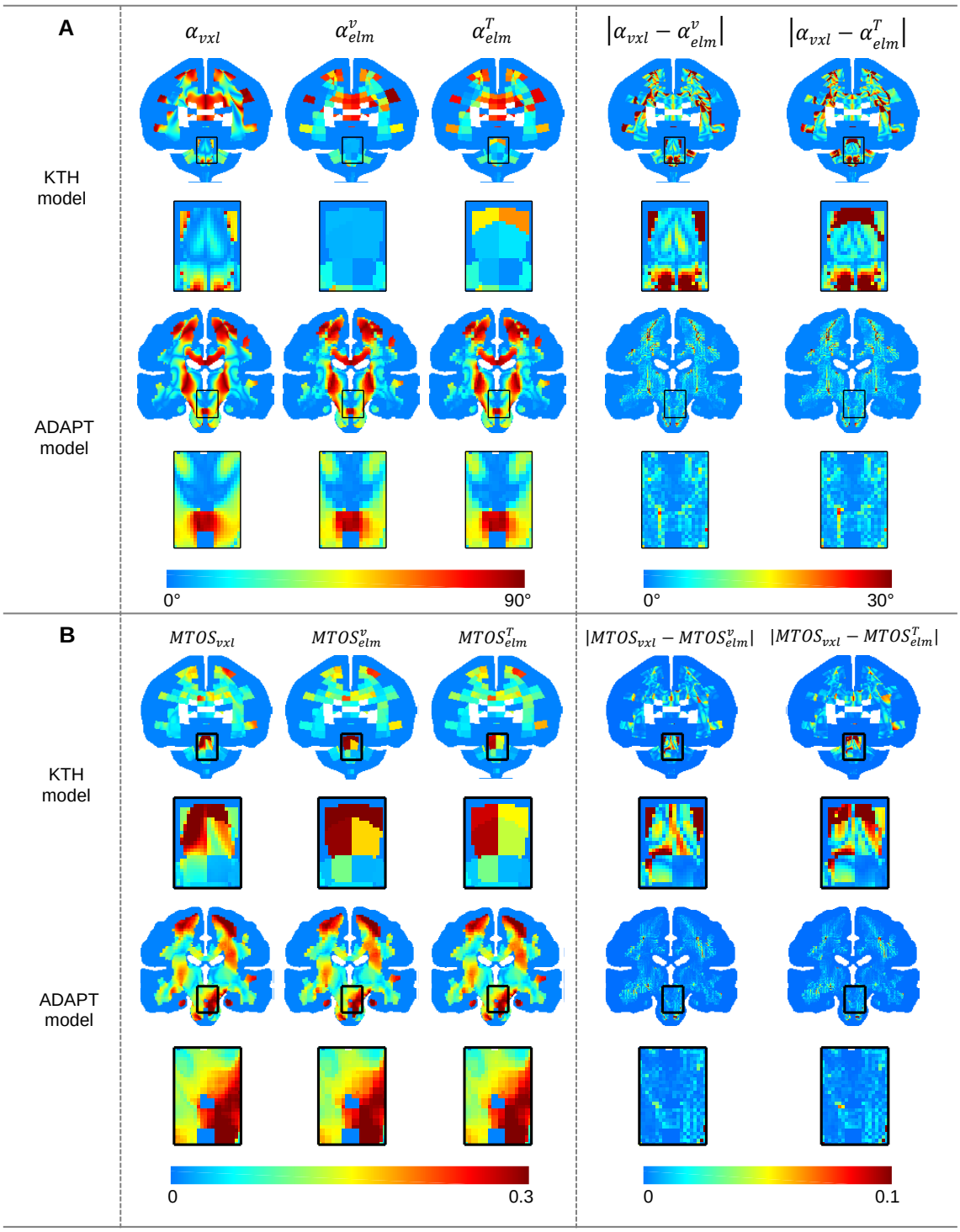

Fig. 7. Coronal cross-sections of elevation angle (α) of fiber orientation (**A**) and MTOS (**B**) determined by the voxel-wise approach and two downsampling approaches along with the absolute difference associated with fiber orientation downsampling. Each cross-section is provided at the whole-brain level along with an enlarged view for the pons regions

Table 2 – NRMSE in tract-related strains associated with fiber orientation downsampling in the KTH and ADAPT models. (**A**) Voxel-wise approach vs. Vector-averaged approach; (**B**) Voxel-wise approach vs. Tensor-averaged approach. The NRMSE values were computed across all WM voxels.

A	NRMSE (%)	KTH model	ADAPT model	**B**	NRMSE (%)	KTH model	ADAPT model

Voxel-wise approach vs. Vector-averaged approach	*MTOS*	33.0	4.2	Voxel-wise approach vs. Tensor-averaged approach	*MTOS*	32.7	4.8
	MTPS	25.0	4.3		*MTPS*	24.5	4.2
	MASS	22.6	3.6		*MASS*	21.7	3.5
	MLSS	20.3	3.3		*MLSS*	20.2	3.3

We further quantified the influence of the orientation downsampling on the peaking response by extracting the 95th percentile value of maximum tract-related strains across the whole WM (**Fig. 8**). For the two downsampling approaches, only minor differences (less than 1%) were noted independent of the strain types and FE models. Comparing with the voxel-wise approach, the tensor-averaged downsampling approach underestimated the peak strains in the KTH model ranging from 6.0% in MTOS to 9.6% in MASS. For the ADAPT model, the differences in the peaking values between the voxel-wise approach and two downsampling approaches were consistently less than 1%.

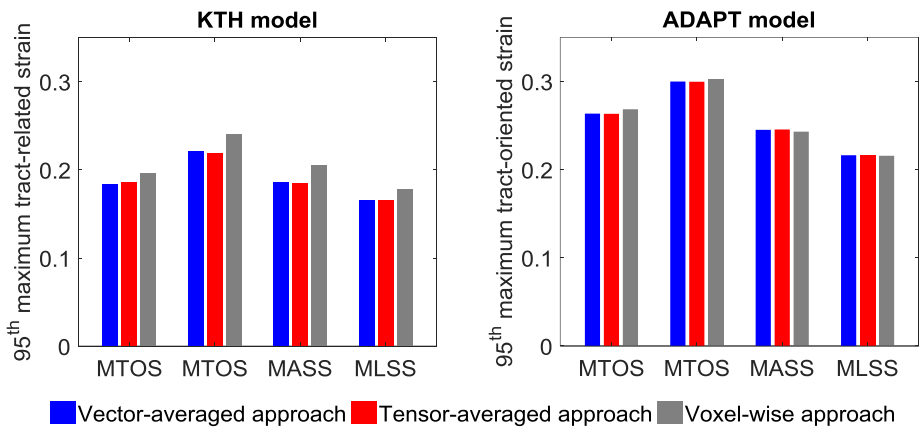

Fig. 8. Comparison of 95th percentile maximum tract-related strains determined by the voxel-wise approach and two downsampling approaches in the KTH and ADAPT models.

Discussions

The current work studied the consequence of fiber orientation downsampling on the tract-related deformation by comparing tract-related strains estimated by a coarsely meshed model and a finely meshed model. For both models, the DTI-delineated fiber orientation was either directly implemented at a voxel-wise basis or at an element-wise basis by two downsampling approaches. By setting the responses from the voxel-wise implementation as the reference, it was verified that, for a model with a large mesh-image resolution, the downsampling orientation exhibited an absolute

difference over 30° across the WM/gray matter interface and pons regions and further negatively affects the computation of tract-related strains with the NRSMR values up to 20% and peaking tract-related strains underestimated by 5% for both downsampling approaches. These downsampling-induced errors are lower in the FE models with finer mesh resolution.

In light of their orientation-dependent natures, tract-related strains require integration of fiber orientation into FE models. Although fiber orientation has been delineated by the DTI technique for decades, the challenge is how to adequately integrate the high-resolution fiber orientation into FE models with varying levels of mesh resolutions. In preference to the element-wise orientation implementation with only one fiber orientation embedded within one WM element (e.g., the vector- and tensor-averaged approaches evaluated in the current work), the voxel-wise approach proposed in the current study addressed the mesh-imaging resolution mismatch by embedding multiple fiber orientation within one element without downsampling. This voxel-wise approach further served as the reference to evaluate the reliability of the vector- and tensor-averaged approaches. As enumerated by the NRMSE values and underestimated peaking strain responses, our work quantified the loss of orientation information due to downsampling and the consequently compromised computation of tract-related strains, which is particularly true for model with coarse meshes.

When comparing the results across all three approaches with and without downsampling, it was found that responses of these two downsampling approaches fell within the range of their counterparts by the voxel-wise approach, as partially demonstrated by one exemplary element per model (**Fig. 6**). Such findings provided certain support to the vector- and tensor-averaged approaches and indicated that the results in previous based on downsampled approaches were not absurdly inaccurate, e.g. the one by Zhou et al. (2021a) using the tensor-averaged approach and the other by Chatelin et al. (2011) using the vector-averaged approach. Despite this, incorporation of the voxel-wise fiber directions without downsampling (e.g., the voxel-wise approach in the current study) provide a more complete configuration of fiber orientation and should be regarded as the rule of thumb.

When limiting the comparison to the results determined by the vector- and tensor-averaged approaches, these two rival schemes performed alike, regardless of the FE models. This was substantiated by the similar distribution and magnitude of orientation information and tract-related strains revealed by these two approaches. Such alike performances were expected given that both practically downsampled the same orientation information from the atlas, with the only difference being the sequence of eigenvector computation and the distance-weighted averaging. For the vector-averaged approach, the principal eigenvectors of tensors in these voxels enclosed by one WM element were computed at first. Then all eigenvectors were averaged by a set of weighting factors based on the distances between the DTI voxels and elemental centroid, outputting a single artificial vector as the mean fiber orientation of the given element. Instead, for the tensor-averaged approach, the tensors of all enclosed DTI voxels were averaged at first with the output as an artificial tensor, and then the principal eigenvector of the artificial tensor was regarded as the mean fiber direction. In the current study, the same weighting factors were used in both averaging approaches, which further explained their similar performances.

Compared with the voxel-wise approach proposed in the current study, another promising approach that could largely leverage the DTI-delineated orientation information is to embed the whole fiber tractography with continuous trajectories into FE models (Garimella, 2017; Hajiaghamemar and Margulies, 2021; Hajiaghamemar et al., 2020; Wu et al., 2019; Zhao et al., 2016). Despite its potential, this approach conforms to multiple challenges associated with tractography reconstruction (Maier-Hein et al., 2017). Thus, the voxel-wise approach proposed in the current study can be regarded as an important alternative to the previous tractography-based efforts, collectively reinforcing further the importance of leveraging the maximum amount of orientation information into the FE models towards an authentic prediction of tract-related deformation.

Limitations and path forward

Although this study yielded insights on how to integrate the neuroimage-delineated fiber orientation into FE models, certain limitations should be acknowledged, which require further investigation. First, besides the vector- and tensor-averaged approaches evaluated in the current study, other orientation downsampling algorithms in the literature can be evaluated in the future. For example, Li et al. (2021) implemented the principal eigenvector from the voxel closest to the centroid of the elemens as the mean fiber direction for the given element, while Kraft and Dagro (2011) regarded the resultant vector by adding the principal eigenvectors of all voxels encased by the element as the mean fiber direction. It is expected that other orientation downsampling algorithms would perform similarly to the vector- and tensor-averaged approaches. Secondly, the current study simulated the brain as an isotropic and homogenous medium, as no complete consensus has been reached yet about the mechanical heterogeneity and anisotropy of the human brain tissue. Relevant limitations have been exhaustively discussed in our recent publications (Zhou et al., 2021a; Zhou et al., 2021b) and are not repeated here. Nevertheless, we acknowledge that evaluating the consequence of orientation downsampling within the context of modelling the brain as an anisotropic and heterogeneous object can be another interesting aspect for future work with the effort initiated by Zhao and Ji (2019b).

Conclusion

The present study proposed a new approach to fully incorporate voxel-wise fiber directions from DTI into FE models and evaluated the reliability of orientation downsampling on tract-related strains. This newly proposed approach and two existing downsampling approaches were implemented into two FE models with varying levels of element sizes, respectively. The orientation downsampling was shown to compromise the accuracy of tract-related strain, particularly for the model with a large mesh-imaging resolution mismatch, while models with refined mesh could partially compensate for the downsampling-induced error. Therefore, this study yields insights on integrating neuroimaging-informed fiber information into FE models to improve the accuracy of FE-derived WM tract-related deformation.

Acknowledgments

This research has received funding from KTH Royal Institute of Technology (Stockholm, Sweden), the China Scholarship Council, the Swedish Foundation for International Cooperation in Research and Higher Education (STINT), and the Swedish Research Council (VR-2020-04496 and VR-2020-04724). The content of this article is solely the responsibility of the authors and does not necessarily represent the official views of funding agencies. The simulation were enabled by resources in project [SNIC 2021/5-406] provided by the Swedish National Infrastructure for Computing (SNIC) at the center for High Performance Computing (PDC), partially funded by the Swedish Research Council through grant agreement no. VR-2020-04496.

Author contributions

Zhou Zhou: Conception and study design, Finite element simulation, Imaging analysis, Data processing, Visualization; Writing – review & editing; **Teng Wang:** Conception and study design, Imaging analysis, Review & editing; **Xiaogai Li:** Conception and study design, Imaging analysis, Review & editing;

Conflict of Interest

The authors declare that they have no conflict of interest.

References

Brazinova, A., Rehorcikova, V., Taylor, M.S., Buckova, V., Majdan, M., Psota, M., Peeters, W., Feigin, V., Theadom, A., Holkovic, L., 2021. Epidemiology of traumatic brain injury in Europe: a living systematic review. Journal of neurotrauma 38, 1411-1440.

Chatelin, S., Deck, C., Renard, F., Kremer, S., Heinrich, C., Armspach, J.-P., Willinger, R., 2011. Computation of axonal elongation in head trauma finite element simulation. Journal of the mechanical behavior of biomedical materials 4, 1905-1919.

Colgan, N.C., Gilchrist, M.D., Curran, K.M., 2010. Applying DTI white matter orientations to finite element head models to examine diffuse TBI under high rotational accelerations. Progress in biophysics and molecular biology 103, 304-309.

De Kegel, D., Meynen, A., Famaey, N., van Lenthe, G.H., Depreitere, B., Vander Sloten, J., 2019. Skull fracture prediction through subject-specific finite element modelling is highly sensitive to model parameters. Journal of the mechanical behavior of biomedical materials 100, 103384.

Fahlstedt, M., Abayazid, F., Panzer, M.B., Trotta, A., Zhao, W., Ghajari, M., Gilchrist, M.D., Ji, S., Kleiven, S., Li, X., 2021. Ranking and rating bicycle helmet safety performance in oblique impacts using eight different brain injury models. Annals of biomedical engineering 49, 1097-1109.

Garimella, H.T., Menghani, R.R., Gerber, J.I., Sridhar, S., Kraft, R.H., 2019. Embedded finite elements for modeling axonal injury. Annals of biomedical engineering 47, 1889-1907.

Garimella, V.R.S.H.T., 2017. An embedded element based human head model to investigate axonal injury. The Pennsylvania State University.

Giordano, C., Cloots, R., Van Dommelen, J., Kleiven, S., 2014. The influence of anisotropy on brain injury prediction. Journal of biomechanics 47, 1052-1059.

Giordano, C., Kleiven, S., 2014. Evaluation of axonal strain as a predictor for mild traumatic brain injuries using finite element modeling. Stapp Car Crash J 58, 29-61.

Giordano, C., Zappalà, S., Kleiven, S., 2017. Anisotropic finite element models for brain injury prediction: the sensitivity of axonal strain to white matter tract inter-subject variability. Biomechanics and modeling in mechanobiology 16, 1269-1293.

Giudice, J.S., Zeng, W., Wu, T., Alshareef, A., Shedd, D.F., Panzer, M.B., 2019. An analytical review of the numerical methods used for finite element modeling of traumatic brain injury. Annals of biomedical engineering 47, 1855-1872.

Hajiaghamemar, M., Margulies, S.S., 2021. Multi-scale white matter tract embedded brain finite element model predicts the location of traumatic diffuse axonal injury. Journal of Neurotrauma 38, 144-157.

Hajiaghamemar, M., Wu, T., Panzer, M.B., Margulies, S.S., 2020. Embedded axonal fiber tracts improve finite element model predictions of traumatic brain injury. Biomechanics and modeling in mechanobiology 19, 1109-1130.

Hernandez, F., Giordano, C., Goubran, M., Parivash, S., Grant, G., Zeineh, M., Camarillo, D., 2019. Lateral impacts correlate with falx cerebri displacement and corpus callosum trauma in sports-related concussions. Biomechanics and modeling in mechanobiology 18, 631-649.

Ho, J., Kleiven, S., 2007. Dynamic response of the brain with vasculature: a three-dimensional computational study. Journal of biomechanics 40, 3006-3012.

Ji, S., Zhao, W., Ford, J.C., Beckwith, J.G., Bolander, R.P., Greenwald, R.M., Flashman, L.A., Paulsen, K.D., McAllister, T.W., 2015. Group-wise evaluation and comparison of white matter fiber strain and maximum principal strain in sports-related concussion. Journal of neurotrauma 32, 441-454.

Kleiven, S., 2006. Evaluation of head injury criteria using a finite element model validated against experiments on localized brain motion, intracerebral acceleration, and intracranial pressure. International Journal of Crashworthiness 11, 65-79.

Kleiven, S., 2007. Predictors for traumatic brain injuries evaluated through accident reconstructions. Stapp car crash J 51, 81-114.

Kleiven, S., von Holst, H., 2002. Consequences of head size following trauma to the human head. Journal of biomechanics 35, 153-160.

Kraft, R.H., Dagro, A.M., 2011. Design and implementation of a numerical technique to inform anisotropic hyperelastic finite element models using diffusion-weighted imaging. ARMY RESEARCH LAB ABERDEEN PROVING GROUND MD WEAPONS AND MATERIALS RESEARCH ….

Kraft, R.H., Mckee, P.J., Dagro, A.M., Grafton, S.T., 2012. Combining the finite element method with structural connectome-based analysis for modeling neurotrauma: connectome neurotrauma mechanics.

Laksari, K., Fanton, M., Wu, L.C., Nguyen, T.H., Kurt, M., Giordano, C., Kelly, E., O'Keeffe, E., Wallace, E., Doherty, C., 2020. Multi-directional dynamic model for traumatic brain injury detection. Journal of neurotrauma 37, 982-993.

LaPlaca, M.C., Simon, C., Prado, G.R., Cullen, D., 2007. CNS injury biomechanics and experimental models. Progress in brain research 161, 13-26.

Li, X., 2021. Subject-specific head model generation by mesh morphing: A personalization framework and its applications. Frontiers in bioengineering and biotechnology.

Li, X., Sandler, H., Kleiven, S., 2017. The importance of nonlinear tissue modelling in finite element simulations of infant head impacts. Biomechanics and modeling in mechanobiology 16, 823-840.

Li, X., Sandler, H., Kleiven, S., 2019. Infant skull fractures: Accident or abuse?: Evidences from biomechanical analysis using finite element head models. Forensic science international 294, 173-182.

Li, X., Zhou, Z., Kleiven, S., 2021. An anatomically detailed and personalizable head injury model: Significance of brain and white matter tract morphological variability on strain. Biomechanics and modeling in mechanobiology 20, 403-431.

Madhukar, A., Ostoja-Starzewski, M., 2019. Finite element methods in human head impact simulations: a review. Annals of biomedical engineering 47, 1832-1854.

Maier-Hein, K.H., Neher, P.F., Houde, J.-C., Côté, M.-A., Garyfallidis, E., Zhong, J., Chamberland, M., Yeh, F.-C., Lin, Y.-C., Ji, Q., 2017. The challenge of mapping the human connectome based on diffusion tractography. Nature communications 8, 1-13.

Mao, H., Gao, H., Cao, L., Genthikatti, V.V., Yang, K.H., 2013. Development of high-quality hexahedral human brain meshes using feature-based multi-block approach. Computer methods in biomechanics and biomedical engineering 16, 271-279.

Maxwell, W., Dhillon, K., Harper, L., Espin, J., MacIntosh, T., Smith, D., Graham, D., 2003. There is differential loss of pyramidal cells from the human hippocampus with survival after blunt head injury. Journal of Neuropathology & Experimental Neurology 62, 272-279.

Montanino, A., 2020. Definition of axonal injury tolerances across scales: A computational multiscale approach. Kungliga Tekniska högskolan.

Mori, S., Oishi, K., Jiang, H., Jiang, L., Li, X., Akhter, K., Hua, K., Faria, A.V., Mahmood, A., Woods, R., 2008. Stereotaxic white matter atlas based on diffusion tensor imaging in an ICBM template. Neuroimage 40, 570-582.

Morrison III, B., Elkin, B.S., Dollé, J.-P., Yarmush, M.L., 2011. In vitro models of traumatic brain injury. Annual review of biomedical engineering 13, 91-126.

Peterson, A.B., Xu, L., Daugherty, J., Breiding, M.J., 2019. Surveillance report of traumatic brain injury-related emergency department visits, hospitalizations, and deaths, United States, 2014. Centers for Disease Control and Prevention, U.S. Department of Health and Human Services, Atlanta, GA, pp. 1-23.

Sahoo, D., Deck, C., Willinger, R., 2014. Development and validation of an advanced anisotropic visco-hyperelastic human brain FE model. Journal of the mechanical behavior of biomedical materials 33, 24-42.

Sahoo, D., Deck, C., Willinger, R., 2016. Brain injury tolerance limit based on computation of axonal strain. Accident Analysis & Prevention 92, 53-70.

Sanchez, E.J., Gabler, L.F., Good, A.B., Funk, J.R., Crandall, J.R., Panzer, M.B., 2019. A reanalysis of football impact reconstructions for head kinematics and finite element modeling. Clinical biomechanics 64, 82-89.

Subramaniam, D.R., Unnikrishnan, G., Sundaramurthy, A., Rubio, J.E., Kote, V.B., Reifman, J., 2021. The importance of modeling the human cerebral vasculature in blunt trauma. Biomedical engineering online 20, 1-19.

Sullivan, S., Eucker, S.A., Gabrieli, D., Bradfield, C., Coats, B., Maltese, M.R., Lee, J., Smith, C., Margulies, S.S., 2015. White matter tract-oriented deformation predicts traumatic axonal brain injury and reveals rotational direction-specific vulnerabilities. Biomechanics and modeling in mechanobiology 14, 877-896.

Wang, T., Kleiven, S., Li, X., 2020. Electroosmosis based novel treatment approach for cerebral edema. IEEE Transactions on Biomedical Engineering 68, 2645-2653.

Wolf, J.A., Johnson, B.N., Johnson, V.E., Putt, M.E., Browne, K.D., Mietus, C.J., Brown, D.P., Wofford, K.L., Smith, D.H., Grady, M.S., 2017. Concussion induces hippocampal circuitry disruption in swine. Journal of neurotrauma 34, 2303-2314.

Wu, T., Alshareef, A., Giudice, J.S., Panzer, M.B., 2019. Explicit modeling of white matter axonal fiber tracts in a finite element brain model. Annals of biomedical engineering 47, 1908-1922.

Wu, T., Hajiaghamemar, M., Giudice, J.S., Alshareef, A., Margulies, S.S., Panzer, M.B., 2021a. Evaluation of tissue-level brain injury metrics using species-specific simulations. Journal of neurotrauma.

Wu, Y.-H., Rosset, S., Lee, T.-r., Dragunow, M., Park, T., Shim, V., 2021b. In Vitro Models of Traumatic Brain Injury: A Systematic Review. Journal of Neurotrauma.

Yang, K., Mao, H., 2019. Modelling of the Brain for Injury Simulation and Prevention, Biomechanics of the Brain. Springer.

Zhan, X., Li, Y., Liu, Y., Domel, A.G., Alizadeh, H.V., Zhou, Z., Cecchi, N.J., Raymond, S.J., Tiernan, S., Ruan, J., Barbat, S., Gevaert, O., Zeineh, M.M., Grant, G.A., Camarillo, D.B., 2021. Predictive Factors of Kinematics in Traumatic Brain Injury from Head Impacts Based on Statistical Interpretation. Annals of Biomedical Engineering.

Zhao, W., Cai, Y., Li, Z., Ji, S., 2017. Injury prediction and vulnerability assessment using strain and susceptibility measures of the deep white matter. Biomechanics and modeling in mechanobiology 16, 1709-1727.

Zhao, W., Ford, J.C., Flashman, L.A., McAllister, T.W., Ji, S., 2016. White matter injury susceptibility via fiber strain evaluation using whole-brain tractography. Journal of neurotrauma 33, 1834-1847.

Zhao, W., Ji, S., 2019a. Mesh convergence behavior and the effect of element integration of a human head injury model. Annals of biomedical engineering 47, 475-486.

Zhao, W., Ji, S., 2019b. White matter anisotropy for impact simulation and response sampling in traumatic brain injury. Journal of neurotrauma 36, 250-263.

Zhao, W., Ji, S., 2020. Incorporation of vasculature in a head injury model lowers local mechanical strains in dynamic impact. Journal of biomechanics 104, 109732.

Zhou, Z., Domel, A.G., Li, X., Grant, G., Kleiven, S., Camarillo, D., Zeineh, M., 2021a. White matter tract-oriented deformation is dependent on real-time axonal fiber orientation. Journal of neurotrauma 38, 1730-1745.

Zhou, Z., Li, X., Kleiven, S., 2019a. Biomechanics of acute subdural hematoma in the elderly: A fluid-structure interaction study. Journal of neurotrauma 36, 2099-2108.

Zhou, Z., Li, X., Kleiven, S., 2019b. Biomechanics of Periventricular Injury. Journal of Neurotrauma 37, 1074-1090.

Zhou, Z., Li, X., Kleiven, S., 2019c. Fluid–structure interaction simulation of the brain–skull interface for acute subdural haematoma prediction. Biomechanics and modeling in mechanobiology 18, 155-173.

Zhou, Z., Li, X., Kleiven, S., Hardy, W.N., 2019d. Brain strain from motion of sparse markers. Stapp car crash journal 63, 1-27.

Zhou, Z., Li, X., Kleiven, S., Shah, C.S., Hardy, W.N., 2018. A Reanalysis of Experimental Brain Strain Data: Implication for Finite Element Head Model Validation. Stapp car crash journal 62, 293-318.

Zhou, Z., Li, X., Liu, Y., Fahlstedt, M., Georgiadis, M., Zhan, X., Raymond, S.J., Grant, G., Kleiven, S., Camarillo, D., 2021b. Towards a comprehensive delineation of white matter tract-related deformation. Journal of neurotrauma 38, 3260-3278.

Appendix

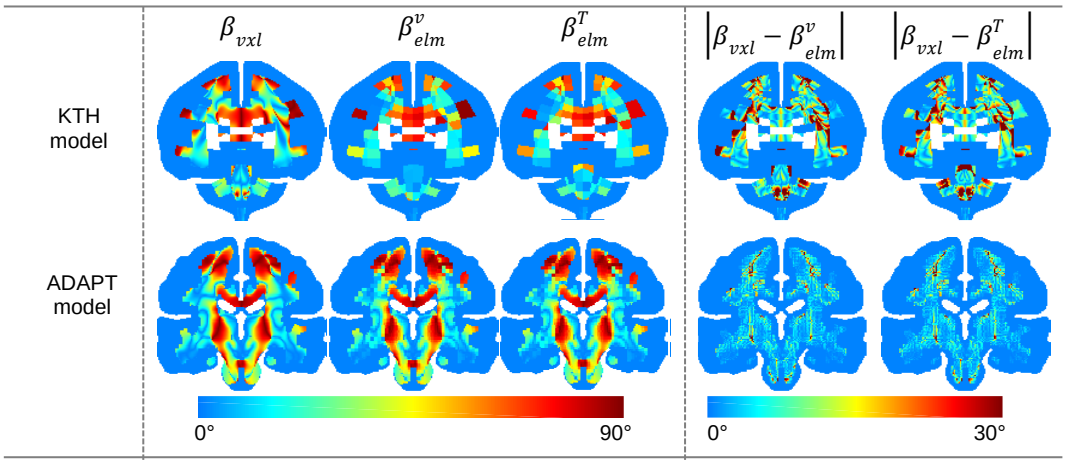

Fig. A1. Coronal cross-sections of azimuth angle (β) of fiber orientation determined by the voxel-wise approach and two downsampling approaches along with the absolute difference associated with orientation downsampling.

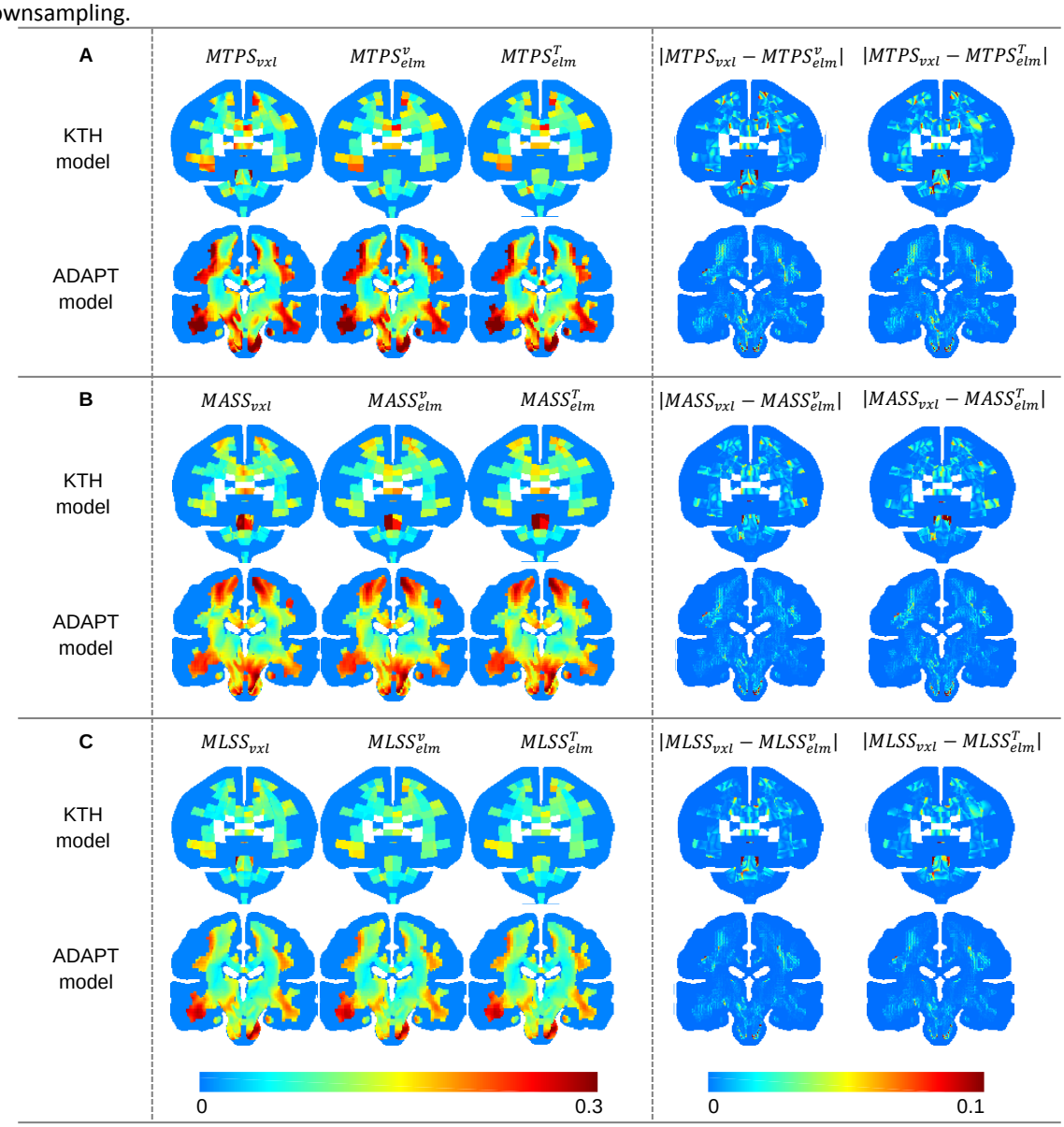

Fig. A2. Coronal cross-sections of MTPS (**A**), MASS (**B**), and MLSS (**C**) determined by the voxel-wise approach and two downsampling approaches along with the absolute difference associated with orientation downsampling.